JGR Atmospheres

RESEARCH ARTICLE
10.1029/2023JD039407

Does a Scale-Aware Convective Parameterization Scheme Improve the Simulation of Heavy Rainfall Events?

Haerin Park[1], Jiwon Hwang[1], Dong-Hyun Cha[1], Myong-In Lee[1], Chang-Keun Song[1], Joowan Kim[2], Sang-Hun Park[3], and Dong-Kyou Lee[4]

[1]Department of Civil, Urban, Earth and Environmental Engineering, Ulsan National Institute of Science and Technology, Ulsan, South Korea, [2]Department of Atmospheric Sciences, Kongju National University, Kongju, South Korea, [3]Department of Atmospheric Sciences, Yonsei University, Seoul, South Korea, [4]School of Earth and Environmental Sciences, Seoul National University, Seoul, South Korea

Key Points:

- We evaluate the impacts of the non-scale-aware and scale-aware convective parameterization scheme (CPS) in the gray-zone using the Weather Research and Forecasting
- The precipitation forecast performance of CPS depends on the type of heavy rainfall event (HRE) and environmental conditions
- The scale-aware CPS in the gray-zone can provide more accurate precipitation forecasts regardless of the environmental condition of the HREs

Correspondence to:
D.-H. Cha,
dhcha@unist.ac.kr

Citation:
Park, H., Hwang, J., Cha, D.-H., Lee, M.-I., Song, C.-K., Kim, J., et al. (2024). Does a scale-aware convective parameterization scheme improve the simulation of heavy rainfall events? *Journal of Geophysical Research: Atmospheres*, *129*, e2023JD039407. https://doi.org/10.1029/2023JD039407

Received 7 JUN 2023
Accepted 20 MAR 2024

Abstract Precipitation predictability using the non-scale-aware and scale-aware convective parameterization schemes (CPSs) was investigated to assess the necessity of the CPSs within the gray-zone. This study evaluates the performance of the Weather Research and Forecasting (WRF) model's CPS for 135 heavy rainfall events (HREs) over the Korean Peninsula for 10 years (i.e., 2011–2020). We tested the Kain–Fritsch (KF) scheme (non-scale-aware) and Multi-scale Kain–Fritsch (MSKF) scheme (scale-aware) in the WRF model. The MSKF scheme shows an overall improved performance of precipitation simulation compared to the KF scheme, but the precipitation forecast performance of CPS depends on the characteristics of HREs. When the HREs are characterized by synoptic-scale atmospheric conditions with strong winds and large-scale water vapor transport, the forecast performance of both CPSs is similar because a cloud microphysics scheme can explicitly resolve most of the precipitation. However, in the case of HREs with weak synoptic forcing conditions (e.g., moisture transport and winds) related to the localized and meso-scale HREs, the MSKF scheme can improve overall simulated precipitation by increasing grid-scale precipitation and reducing the overestimation of subgrid-scale precipitation simulated in the KF scheme. Therefore, using the scale-aware CPS in the gray-zone can provide more accurate precipitation forecasts regardless of the environmental condition of the HREs.

Plain Language Summary In this study, we evaluate the predictability of precipitation using two types of convective parameterization schemes (CPS), non-scale-aware and scale-aware, in the Weather Research and Forecasting (WRF) model. The scale-aware CPS utilizes scale-aware parameters to adjust convection processes based on horizontal resolution. We focus on heavy rainfall events (HREs) over the Korean Peninsula for 10 years from 2011 to 2020. A HRE is defined as rainfall greater than 110 mm in 12 hr. The results show that the scale-aware CPS improved the precipitation forecast performance compared to the non-scale-aware CPS, and the precipitation forecast performance of CPS differs depending on the characteristics of HREs. For HREs characterized by the synoptic forcing conditions with strong winds and large-scale horizontal advection of water vapor, both CPSs perform well, but their forecast performance decreases for HREs with weak synoptic forcing conditions. We also find that for localized heavy rain cases, using the scale-aware CPS helps improve precipitation forecasts at 4-km horizontal resolution.

1. Introduction

In the Korean Peninsula, precipitation is concentrated during the summer monsoon, with more than half the annual rainfall occurring. The summer monsoon season, known as "Changma," typically occurs from June to September and is one of the destructive characteristics of extreme precipitation, causing considerable socio-economic damage. In addition, the Korean Peninsula can also experience extremely heavy rainfall events from other weather systems, including the interaction between surface- and upper-level low-pressure systems, the development of mesoscale convective systems, and typhoon activity (Cho & Lee, 2006; Deuk-Kyun et al., 2005; Shin & Lee, 2005; Sun & Lee, 2002). Precipitation processes of various scales, from synoptic-scale rainfall covering the entire Korean Peninsula to small-scale rainfall caused by localized precipitation processes (e.g., orographic effects, buoyant instabilities, etc.), affect the region (Lee & Kim, 2007). Recent trends in summer precipitation on the Korean Peninsula show shorter duration and increasing intensity, with localized precipitation limiting the model's predictability (Kim et al., 2020). To reduce the damage caused by heavy rainfall in Korea,

more reliable and accurate predictions based on numerical models are necessary, along with an increased understanding of heavy rainfall events (HREs).

In many previous studies, numerical models have used a coarse horizontal grid spacing relative to the actual size of convective clouds owing to limitations in computing resources. As a result, the convective parameterization schemes (CPS) have been typically utilized in numerical weather prediction (NWP) models to implicitly represent unresolved convection, much smaller than the coarse horizontal grid size of approximately 10 km. However, recent advancements in numerical computing power and atmospheric modeling techniques have enabled NWP models to simulate the atmosphere at a sub-kilometer scale (Charles & Colle, 2009; Davies et al., 2005; Saito et al., 2006). When using CPS at a fine resolution, some critical cumulus assumptions and simplifications may break down, considerably diminishing the quality of the forecast. This issue has been suggested as a problem with using CPSs at 1–10 km, referred to as the "gray-zone", where convection is neither explicitly fully resolved nor fully parameterized.

In general, many studies have shown that it may not be necessary to use CPS for grid spacing finer than 5 km (Jee & Kim, 2017; Liang et al., 2019; McMillen & Steenburgh, 2015). However, some studies have indicated that using the CPS and cloud microphysics schemes (MPS) may be necessary for improved forecasts of heavy rainfall and mesoscale convective systems (MCSs) at grid-scales of 3–4 km (Deng & Stauffer, 2006; Lee et al., 2011; Park et al., 2022). Overall, the question of whether it is beneficial to use CPS within a resolution of 5 km is still being determined and may depend on the type of CPSs as well as the environmental condition (e.g., correctness of initial and boundary conditions) and also on the other physics parametrizations (e.g., surface, boundary layer, radiation, cloud fraction).

Thus, the physical process of the scale-aware CPS, which is adjusted according to changes in model resolution, has become an important direction for the development of NWPs to reduce ambiguity about using CPS in the gray-zone (Arakawa et al., 2011; Bengtsson & Körnich, 2016; Gerard et al., 2009; Grell & Freitas, 2014; Hong & Dudhia, 2012; Han & Hong, 2018; Han et al., 2017; Park, 2014; Prein et al., 2015; Yun et al., 2017; Zheng et al., 2016). To improve gray-zone precipitation forecasts, Zheng et al. (2016) developed the Kain-Fritsch (KF) scheme by adjusting parameters that depend on the horizontal resolution to modify the adjustment time scale and entrainment processes. Kwon and Hong (2017) also improved precipitation simulation on the Korean Peninsula using the Simplified Arakawa–Schubert scheme with scale recognition parameters applied at a resolution of 3 km. Park et al. (2022) suggested not only the limitation of only MPS without CPS, but also the need for a scale-aware CPS within a high resolution (e.g., 4 km) by comparing the non-scale-aware CPS (Kain-Fritsch, KF), scale-aware CPS (Multi-scale Kain-Fritsch, MSKF), and only MPS without CPS for a MCS case on the Korean Peninsula. They showed that the scale-aware parameter within CPS in the gray-zone could play an important role in balancing the effects of the CPS and MPS by regulating the triggering and development of convection. These efforts aim to develop a CPS that can automatically adjust its role based on grid spacing and improve precipitation forecasts at high resolutions.

Hong (2004) found that the traditional (i.e., non-scale-aware) CPS could have a negative impact on precipitation simulation because the summer season in Korea has strong baroclinic characteristics related to synoptic-scale features (e.g., extratropical cyclones and the quasi-stationary frontal system). In addition, most assessments of the accuracy of scale-aware CPS in predicting precipitation on the Korean Peninsula have been limited to single case studies (Kwon & Hong, 2017; Park et al., 2022).

Therefore, this study investigated the generalized predictability of the CPS for HREs on the Korean Peninsula in the gray-zone using the Advanced Research Weather Research and Forecasting (WRF) model (Skamarock et al., 2019). In addition, we suggested the need for a scale-aware CPS in the gray-zone by comparing it with the non-scale-aware CPS. In this study, the KF (Kain, 2004) and MSKF schemes (Zheng et al., 2016) were selected as the non-scale-aware and scale-aware CPS, respectively, and tested for the cases of heavy rainfall on the Korean Peninsula during the summer (from June to September) from 2011 to 2020. The remainder of the manuscript is organized as follows. First, the HREs and design of the numerical experiments are described in Section 2. Next, the results of the numerical experiments with different CPSs are presented in Section 3. Finally, a summary and conclusions are given in Section 4.

2. Data and Method

2.1. Identification of HREs

The hourly precipitation data recorded at the Automated Synoptic Observing Systems (ASOS) of the Korea Meteorological Administration (KMA) were used to select HREs during the summer and early autumn months (June, July, August, and September) between 2011 and 2020. In this study, an HRE was defined by the KMA heavy rainfall criteria as an event with 12-hr rainfall accumulations >110 mm at any single ASOS station: this definition is the KMA's HRE warning criteria. Even if an HRE is observed multiple times at various stations within 12-hr, it is considered a single HRE. A total of 135 HREs were selected after excluding those caused by the direct influence of typhoons. Such events are determined by the date provided in the Korean Peninsula Typhoon Analysis Report (2011–2020). The reference time of each HRE is defined as the center of the 12-hr window of the accumulated rainfall, for example, 0600 UTC for 12-hr accumulated precipitation during 0000–1200 UTC.

2.2. Data

Six-hourly National Centers for Environmental Prediction/National Centers for Atmospheric Research (NCEP/NCAR) GDAS final analysis (FNL) data (https://rda.ucar.edu/datasets/ds083.2/) at a $1° \times 1°$ horizontal resolution is used for the initial and lateral boundary conditions of the WRF model. To evaluate the precipitation from the simulated results, a half-hourly Integrated Multi-SatelliE Retrievals for Global Precipitation Measurement (IMERG, Huffman, Bolvin, Braithwaite, et al., 2015, Huffman, Bolvin, Braithwaite, et al., 2015) data at a $0.1° \times 0.1°$ horizontal resolution is used. The higher resolution model results (i.e., WRF model result in 4-km resolution) are converted to the IMERG grid using bilinear interpolation. We also use the six-hourly fifth generation of atmospheric reanalysis (ERA5) data (Hersbach et al., 2020) at a $0.25° \times 0.25°$ horizontal resolution released by the European Centre for Medium-Range Weather Forecasts (ECMWF) to analyze the environmental conditions of the HREs.

2.3. Numerical Experiments

We use the WRF model Version 4.1. The FNL data is used to provide the initial and boundary conditions for the WRF model, with a grid spacing of $1° \times 1°$. Here, we consider only one initial condition. We use multiple two-way nesting domains with Lambert conformal map projection. The domains consist of different horizontal grid spacings of 36 km (201 × 201), 12 km (352 × 352), and 4 km (460 × 460), including the CPS in gray-zone resolution (Figure 1). All simulations lasted 48-hr from the model initiation; the simulation is initiated 36-hr before the reference time of HRE and finalized 12-hr after the reference time. The physical parameterization schemes used are the Yonsei University planetary boundary layer scheme (Hong et al., 2006; Noh et al., 2003), the WSM6 cloud microphysics scheme (Hong & Lim, 2006), the Dudhia shortwave radiation scheme (Dudhia, 1989) and the longwave radiation scheme based on the rapid radiative transfer model (Mlawer et al., 1997), and the unified Noah land-surface model (Chen & Dudhia, 2001; Ek et al., 2003). In this study, the KF and MSKF schemes are employed as CPSs. To investigate the effect of CPSs in the gray-zone, we use the CPSs in all domains.

The KF scheme is a subgrid scheme that uses a mass flux technique to compute the CAPE-based closure assumption system by parameterizing convections. The MSKF scheme is a scale-aware version of the KF scheme. It incorporates parameterized cloud dynamics for high-resolution forecasts by modifying the KF scheme, including cloud fraction adjustments (Alapaty et al., 2012, 2014) and the adjusted grid-scale velocity expressed in terms of the subgrid-scale updraft mass flux. Other scale-dependent parameters include the fallout rate of condensates. The MSKF scheme also includes changes in the convective adjustment timescale and improvements in entrainment formulations (Zheng et al., 2016). A recent study (Park et al., 2022) showed that the MSKF scheme, with its improved convective adjustment timescale and entrainment formulations, yielded significant improvements in the forecast accuracy of meso-scale convective cells in South Korea.

This study is designed to evaluate WRF skills in simulating HREs for two different convective schemes (non-scale-aware KF and scale-aware MSKF) for the purpose to reducing the ambiguity of using CPS in simulating precipitation over the Korean Peninsula within the gray-zone.

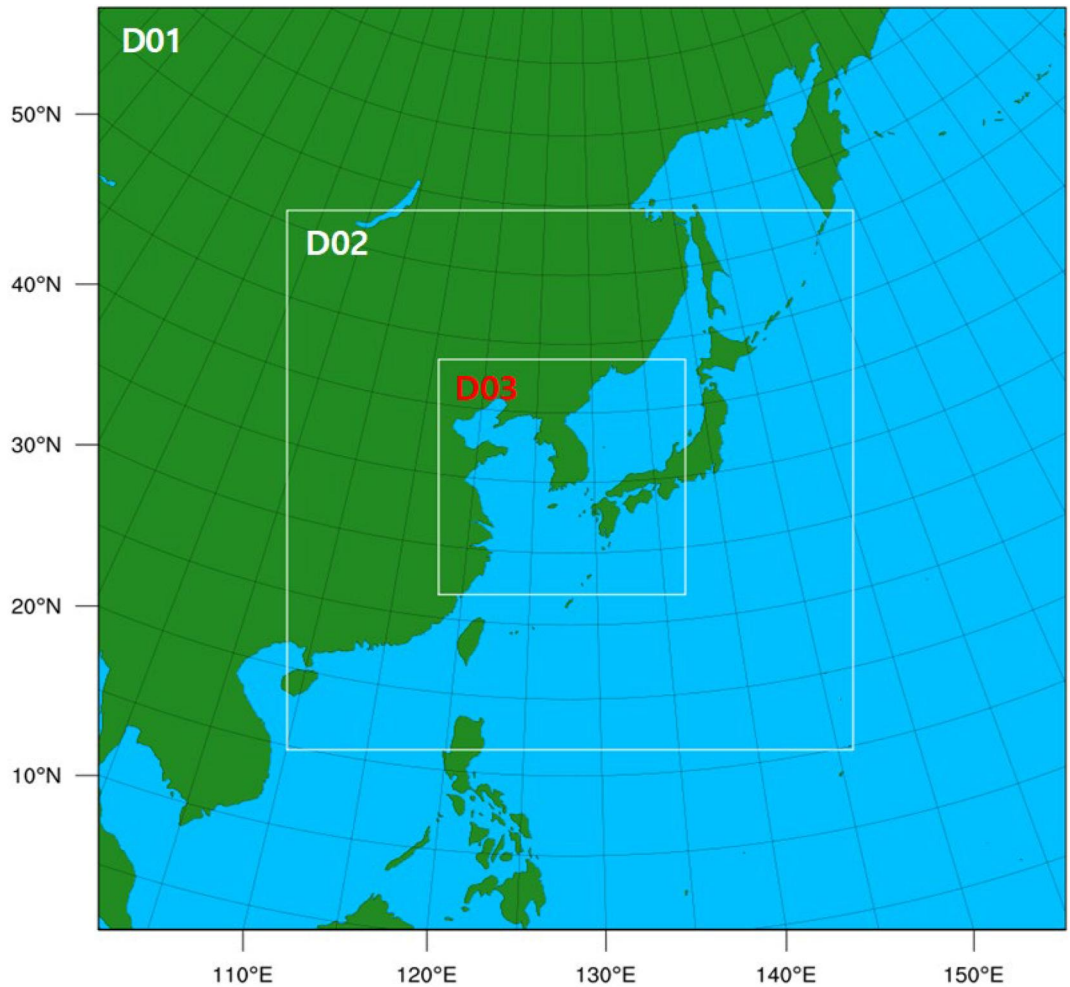

Figure 1. Map showing three nested domains with 36, 12, and 4 km grid spacings in WRF.

3. Results

The investigations conducted in this study consist of two parts. First, we evaluate the overall performance of precipitation simulations between KF and MSKF schemes for 135 HREs. Subsequently, to examine the causes of the difference in the simulations among the two schemes, we analyze the synoptic forcing of HREs based on the ERA5 reanalysis data.

3.1. Assessment of the Impact of CPSs

Differences in precipitation forecasts between the KF and MSKF experiments are analyzed by calculating the forecast skills with respect to the IMERG data. We calculate four standard skill scores (i.e., the probability of detection, POD, threat score, TS, false alarm ratio, FAR, and bias score, BS) for precipitation with various intensity thresholds (e.g., 5, 10, 20, 30, 50,70, and 110 mm). Note that a POD, TS, and BS close to 1 and FAR close to 0 indicate better forecast performance. The simulated precipitation on the D03 domain (i.e., 4 km) are interpolated to the grid points of the observation (i.e., IMERG data), and model statistics are calculated for the target region (between 30–45°N and 120–135°E) using Equations 1–4 (Wilks, 2011).

$$\mathrm{POD} = \frac{H}{H + M}, \tag{1}$$

$$\mathrm{TS} = \frac{H}{H + F + M} \tag{2}$$

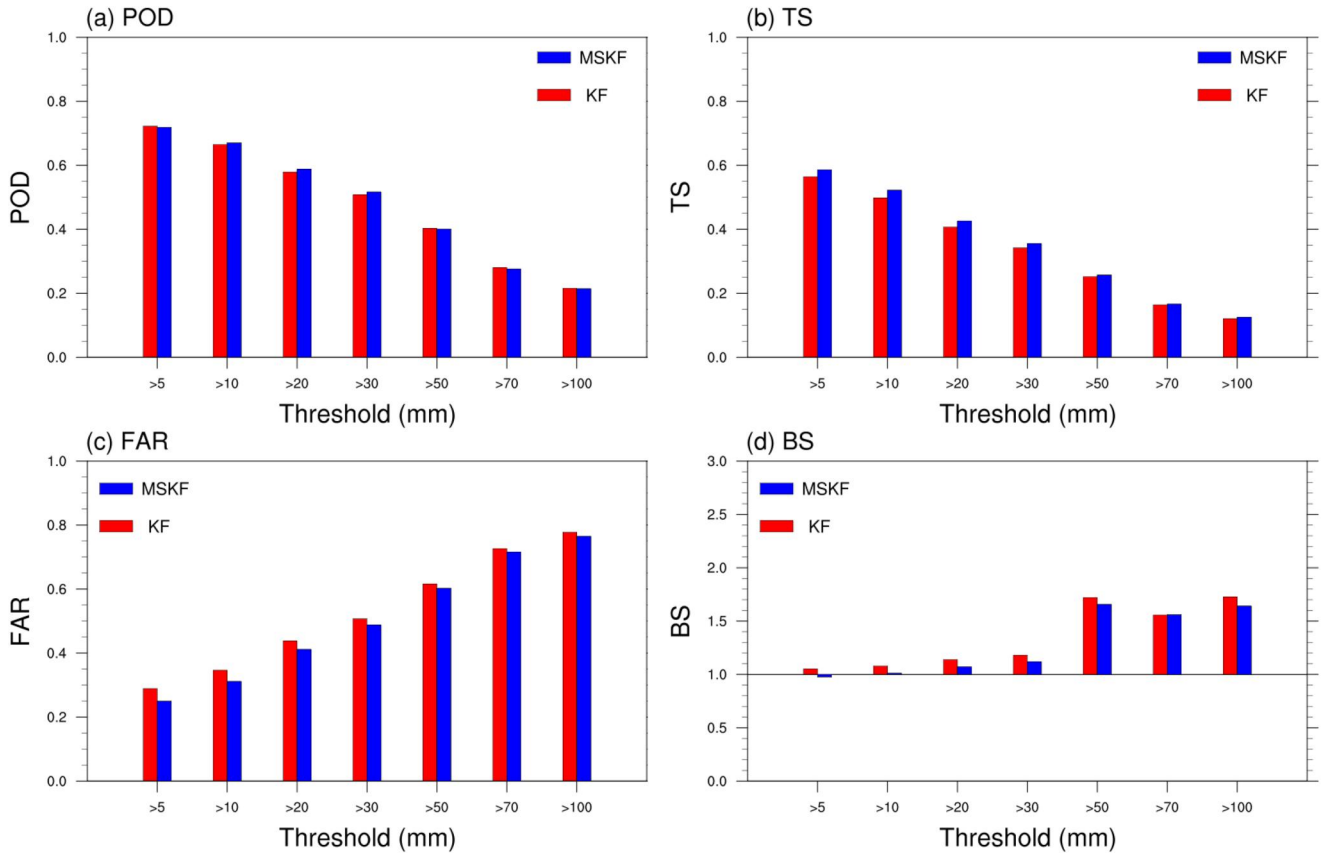

Figure 2. Bar plots of the statistical indices corresponding to the KF and MSKF experiments with the IMERG data based on different thresholds of 48-hr accumulated precipitation. Simulated precipitation is interpolated to the observation grid points, and model statistics are calculated for South Korea and the Yellow Sea (between 30 and 45°N and 120–135°E). Simulated precipitation is calculated from the results of the 4-km resolution domain.

$$\mathrm{FAR} = \frac{F}{H+F}, \text{and} \tag{3}$$

$$\mathrm{BS} = \frac{H+F}{H+M} \tag{4}$$

Here, "H" are hits, "F" are false alarms, "M" are misses. "H" is the number of correct precipitation forecasts. These are calculated in units of grid boxes within the target region. "M" is defined when precipitation is detected by the IMERG data but not by the WRF model. "F" is defined when the WRF model predicts precipitation, but there is no detection in the IMERG data.

Figure 2 shows the average skill scores of 48-hr precipitation forecasts over the target area for 135 HREs. In both experiments, the skill scores tend to decrease with increasing threshold. We conduct paired *t*-test statistical analysis (with a significant level of $p < 0.05$) to evaluate the statistical significance of the two-system performance and find that there are significant differences in all thresholds and verification indices, and especially, the performance improvement of MSKF is particularly noticeable at lower precipitation thresholds (*t*-test value is not shown). Furthermore, as the precipitation threshold decreases, the difference between the MSKF and KF experiments becomes more pronounced in the three verification measures (TS, FAR, and BS) that used the "F" indices. Based on a BS (Figure 2d), the KF experiments overestimate the precipitation (i.e., BS > 1) across the entire range of precipitation thresholds, suggesting that the KF has more "false alarms" than "misses." On the other hand, the MSKF experiments slightly underestimate light precipitation (i.e., >5 mm) but overestimate moderate and heavy precipitation (i.e., >10, 20, 30, 50, 70, and 100 mm). In addition, the difference in FAR between the two experiments significantly increases with decreasing threshold (Figure 2c), indicating that the KF

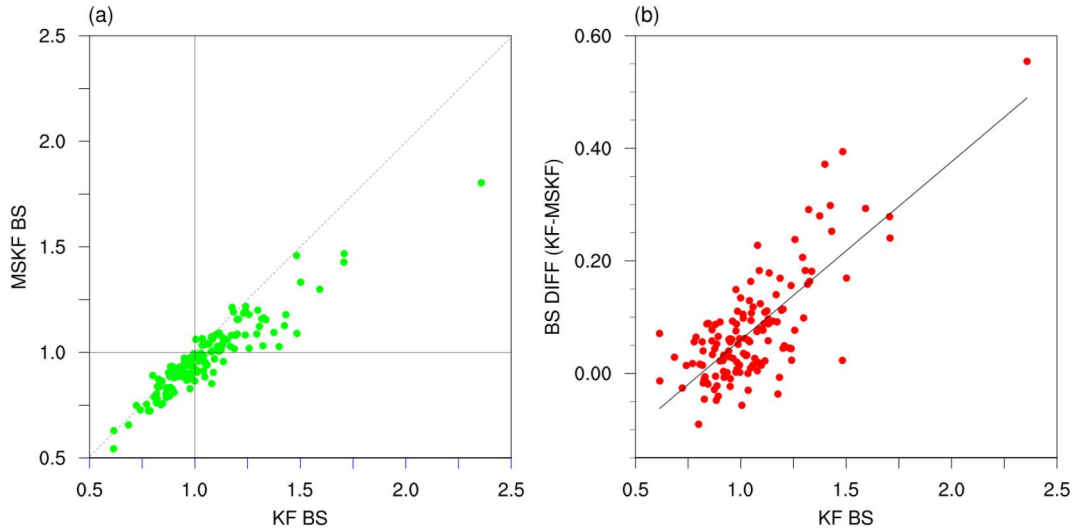

Figure 3. Scatter plot of BS of the KF and (a) MSKF experiments for 135 HREs, (b) BS difference between the MSKF and KF experiments for 135 HREs. BS indices corresponding to the KF and MSKF experiments with IMERG data based on thresholds (>5 mm) of 48-hr accumulated precipitation. Model statistics are calculated for target region (between 30 and 45° N and 120–135°E). Simulated precipitation is calculated from the results of the 4-km resolution domain.

experiments tend to simulate more "F" rather than "H" compared to the MSKF experiments as the threshold is lower. This result is similar to that of the BS. It implies that the KF scheme tends to simulate more precipitation than the MSKF scheme, and the tendency is especially evident at light precipitation thresholds. Park et al. (2022) suggest that CPS overpredicts light precipitation in the gray-zone, which can lead to inaccurate simulations of heavy precipitation because the overestimation of light precipitation can unrealistically strengthen the lower-level wind field and water vapor transport. The predictability of light precipitation in CPS can impact the accuracy of heavy precipitation prediction. Therefore, the remainder of this study investigates the predictability of precipitation between KF and MSKF schemes by using a threshold of 5 mm.

Figure 3a shows a scatter plot of the BS of the two schemes for 135 HREs when the 48-hr accumulated precipitation threshold is 5 mm. For most HREs, the BS values in the KF experiments tend to be higher than those in the MSKF experiments, although the overall trend of the BS is similar in both experiments. This means that the KF scheme overestimates rainfall in more HREs compared to the MSKF scheme; for the 128 HREs, the KF experiments have higher BS than the MSKF experiments ($p < 0.001$). In Figure 3b, a scatter plot of the BS in the KF experiments and the difference in BS between the two experiments are shown to clarify the relationship between the errors of the KF experiments and the predictability difference. The results represent that the predictability difference between the two experiments tends to increase as the BS of the KF experiments increases, with a correlation coefficient of 0.57 ($p < 0.001$). In other words, the improvement in precipitation simulation by the MSKF scheme can be large as the precipitation overestimated by the KF scheme increases.

To investigate the trends in precipitation predictability for CPSs and understand the differences between them, we analyze the synoptic forcing around the Korean Peninsula. Previous studies have shown that the LLJ is closely related to heavy rainfall over East Asia in summer and is an important synoptic forcing for heavy rainfall over the Korean Peninsula (Chen & Yu, 1988; Hwang, 1993; Jeong & Ryu, 2008; Matsumoto, 1973). The formula for kinetic energy (KE) is $0.5^* \sqrt{u^2 + v^2}$, which is similar to the wind speed. Therefore, we represented the synoptic forcing using KE. KE is defined as the spatial average over the target region at the reference time of HREs at certain level (hPa). First, to understand the synoptic conditions that have a large impact on the precipitation predictability of CPS, scatter plots of KE at 200 hPa and 700 hPa levels are made against pattern correlation (PC) and root mean squared error (RMSE) of 48-hr accumulated precipitation between WRF simulations and IMERG data (Figure 4). The PC is given by

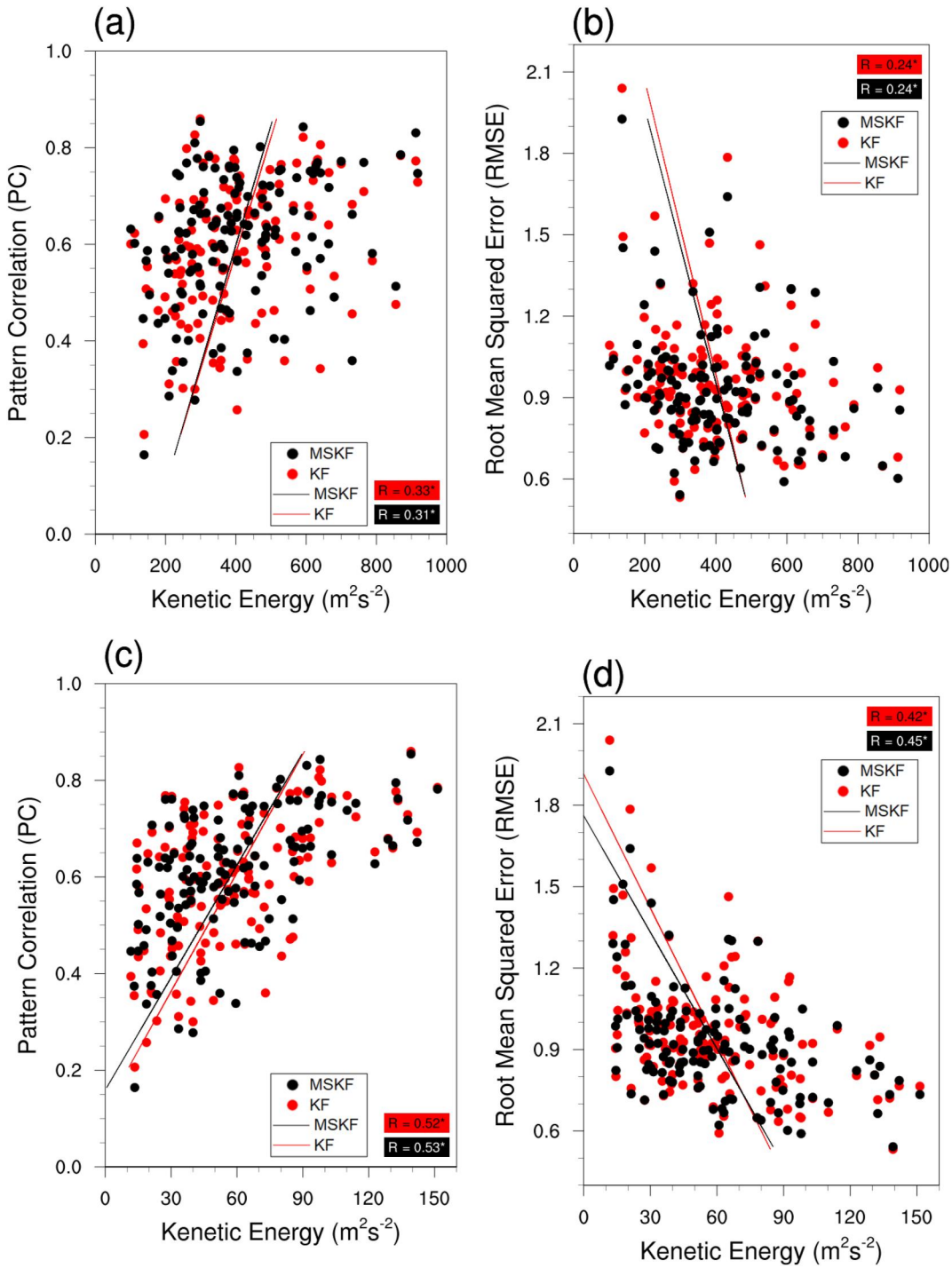

Figure 4. The relationship between the (a,c) pattern correlation (PC) and (b,d) root mean squared error (RMSE) of the KE ($m^2\ s^{-2}$) at (a, b) 200 hPa and (c, d) 700 hPa, as determined by the CPSs. (* represents $p < 0.001$).

$$PC = \frac{\sum_{i}^{N}\left(X_{imerg,i} - \overline{X}_{imerg}\right)\left(X_{model,i} - \overline{X}_{model}\right)}{\sqrt{\sum_{i}^{N}\left(X_{imerg,i} - \overline{X}_{imerg}\right)^2}\sqrt{\sum_{i}^{N}\left(X_{model,i} - \overline{X}_{model}\right)^2}} \quad (5)$$

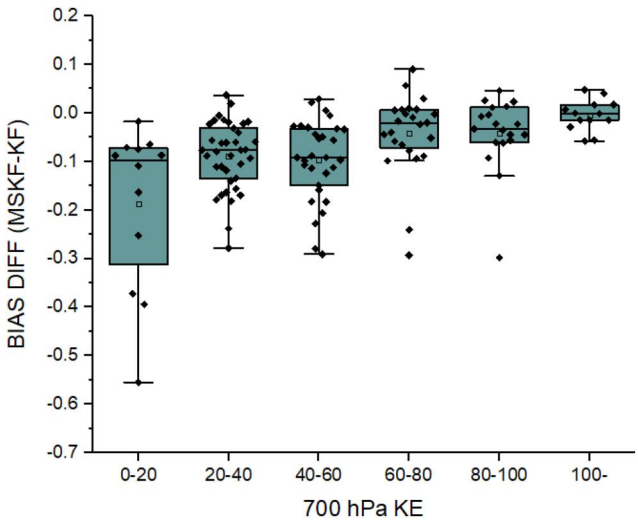

Figure 5. Box plot of BS difference for various thresholds of KE ($m^2\ s^{-2}$) at 700 hPa. BS indices corresponding to the KF and MSKF experiments with IMERG data based on thresholds (>5 mm) of 48-hr accumulated precipitation. Error bars represent the spread between the 25th and 75th percentiles.

where N is the total number of grid boxes for WRF predictions and observed data, X_{imerg} (X_{model}) represents the IMERG data (WRF prediction), $\overline{X}_{imerg}$ ($\overline{X}_{model}$) is the mean of the IMERG data (WRF prediction). The range of the pattern correlation, calculated using Equation 5, is from zero to 1. PC of 1 indicates perfect linear correlation between the data, while PC of 0 indicates no linear correlation.

PC and RMSE are selected to analyze the simulation performance of WRF in terms of distribution and intensity of precipitation, respectively. Both experiments show a tendency to decrease PC and increase RMSE, respectively, as KE decreases. This means that the weaker synoptic forcing of HREs can be associated with the lower precipitation prediction performance. The correlation between the upper-level KE in the two experiments and the two statistics is not significantly high. On the other hand, the correlation of the lower-level KE in the KF (MSKF) experiments with the PC was 0.53 (0.52), and the correlation with the RMSE was 0.45 (0.42). This implies that the performance of the two schemes is more affected by the lower-level atmospheric environment than the upper-level environment. From this, we confirm that the precipitation predictability of the CPS is more highly correlated with KE at lower-level than with that at the upper-level.

To further investigate the relationship between synoptic forcing and the difference in predictability between CPSs, we analyze the relationship between BS differences (MSKF-KF) and lower-level KE in two experiments (Figure 5). When the KE is less than 40 $m^2\ s^{-2}$, the predictability differences among HREs had a spread of approximately 0.6 ($-0.55 \sim 0.50$), but when the KE exceeded 100 $m^2\ s^{-2}$, the spread became relatively small, about 0.1 ($-0.05 \sim 0.05$). This suggests that the environmental characteristics of the synoptic forcing can determine the performance of precipitation simulation by CPS. As KE decreases, the predictability difference between CPSs increases, while as KE increases, the predictability similarity between CPS increases. In order words, the weaker synoptic forcing conditions, the larger predictability difference between the MSKF and KF schemes. The result implies that the MSKF scheme can play a significant scale-aware role when there are no dominant synoptic forcing conditions.

3.2. Synoptic Characteristics of HREs in LARGE and SMALL

To investigate the scale-aware effect of the MSKF scheme, we classify HREs into two groups based on the difference in the predictive performance of the two schemes and analyze the environmental characteristics of each group. In particular, we select 10 HREs with significant differences in predictability (i.e., BS) and 10 HREs with slight differences in predictability, which we call "LARGE" and "SMALL" groups, respectively. We analyze the synoptic pattern based on the reanalysis data to investigate the causes of the difference in the simulations between the LARGE and SMALL cases. Figure 6 shows the composite map representing the synoptic pattern of HREs in the LARGE and SMALL cases using ERA5 reanalysis data. The composite map is represented by averaging the reanalysis data at the reference time of HREs mentioned in Section 2.1. The composite map of the SMALL cases shows a wide region with a high equivalent potential temperature (θ_e) at 500 hPa from Shanghai (30°N, 120°E) to the central part of the Korean Peninsula, thus the strong north-south gradient of θ_e appears over the Korean Peninsula (Figure 6a). The boundary of the western North Pacific subtropical high (WNPSH) defined by the 5880-gpm contour (e.g., Ren et al., 2015; Seo et al., 2011) expands to southwestern Japan. In addition, a relatively large amount of moisture (>600 kg $m^{-1}\ s^{-1}$) is transported along the WNPSH boundary toward the Korean Peninsula (Figure 6c). The moist transport is represented by the integrated water vapor transport (IVT) using the following equation:

$$\mathrm{IVT} = \left(-\frac{1}{g}\int_{1000\ hPa}^{300\ hPa} uqdp\right) + \left(-\frac{1}{g}\int_{1000\ hPa}^{300\ hPa} vqdp\right), \quad (6)$$

where g is the gravitational acceleration, u and v are the zonal and meridional winds, respectively, q is the specific humidity, and p is the atmospheric pressure.

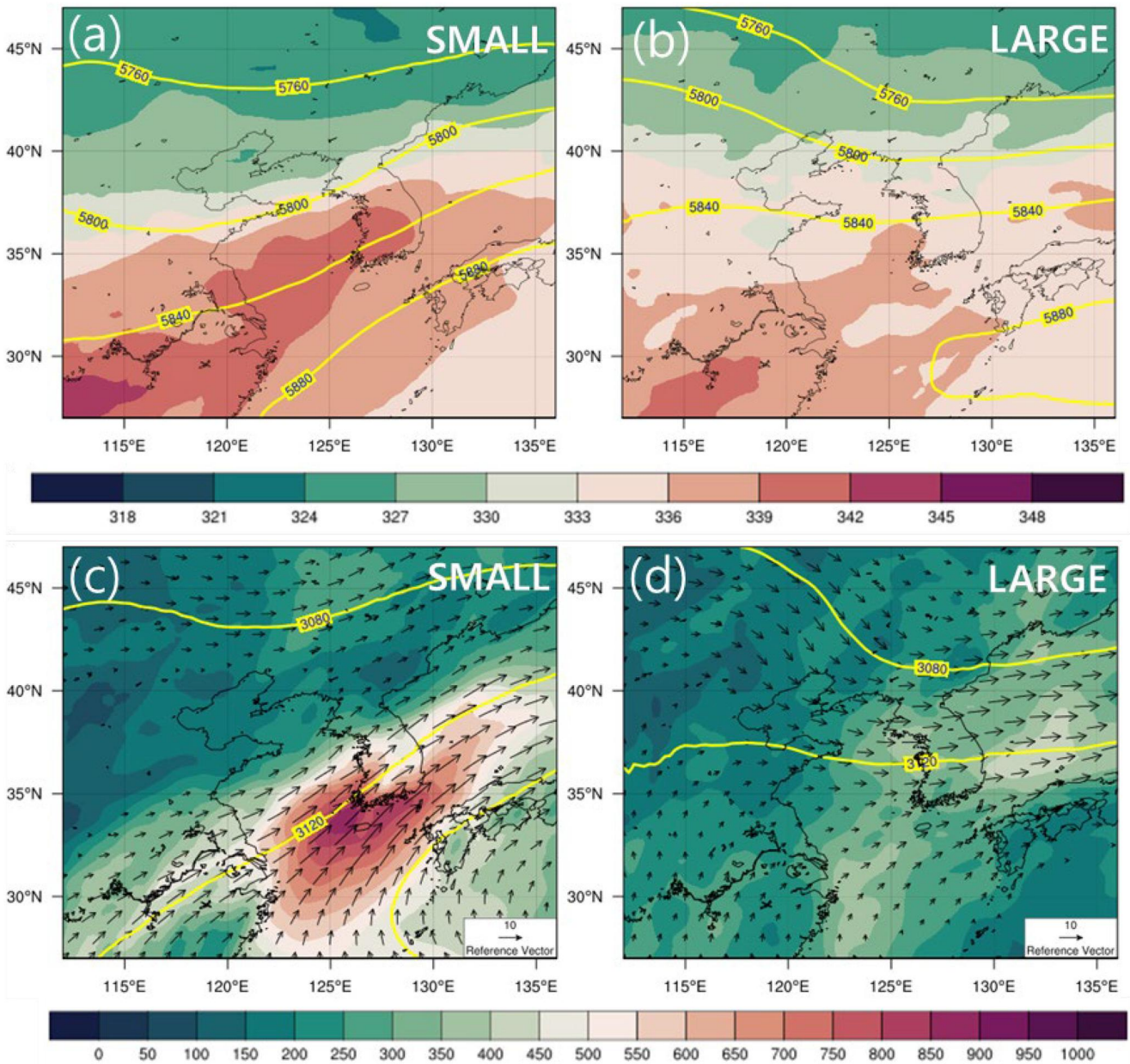

Figure 6. Composited synoptic structures of 10 HREs in the SMALL and LARGE cases. (a–b) GPH (gpm, contours) and equivalent potential temperature (K, shading) at 500 hPa and (c–d) IVT (kg m^{-1} s^{-1}, shading), and GPH (gpm, contours) and wind vector (>5 m s^{-1}, vector) at 700 hPa.

On the other hand, the HREs in the LARGE cases show notably different environmental features from those in the SMALL cases (Figures 6b and 6d). The WNPSH is prominently shrunken to the east in the LARGE cases compared to that in the SMALL cases, and the north-south gradient of θ_e around the Korean Peninsula also decreases. In addition, the amount of water vapor transported into the Korean Peninsula significantly decreases (IVT < 500 kg m^{-1} s^{-1}) due to the reduced southwesterly winds. These results imply that the HREs in the SMALL and LARGE cases are differentiated in terms of their synoptic patterns; strong southwesterly moisture transport along the northwestern edge of the WNPSH for the SMALL cases, but no distinct synoptic forcings (e.g., moisture transport and strong winds) for the LARGE cases.

To investigate the influence of CPSs on the precipitation simulation, we select five representative HREs in the SMALL and LARGE cases (not shown for the other five cases). We analyze the differences in precipitation distribution and the role of CPSs for each case. Figures 7 and 8 show the spatial distribution of 48-hr accumulated

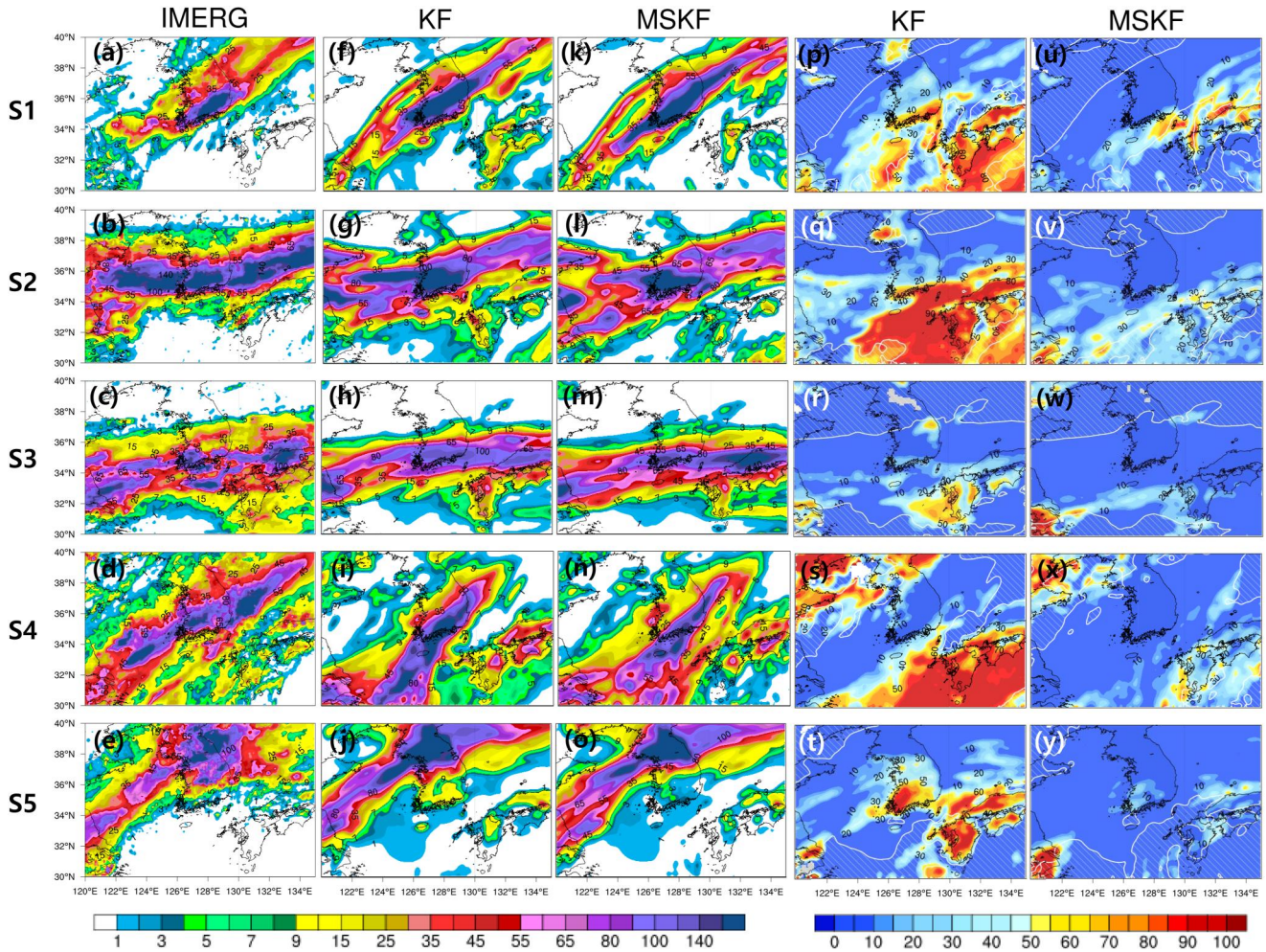

Figure 7. Spatial distribution of (a–o) 48-hr accumulated total precipitation (mm) in the D03 domain and (p–y) CRR (%) for five representative HREs in the SMALL cases. White dashed line indicates the areas where total precipitation is less than 1 mm.

precipitation (a-o) and convective rain ratio (CRR, p-y) for five representative HREs, in the SMALL and LARGE cases, respectively. The WRF model allows the separation of total precipitation into subgrid-scale and grid-scale precipitation through CPS and MPS, respectively.

$$\mathrm{CRR} = \frac{subgrid - scale\ precipitation}{total\ precipitation} \tag{7}$$

As shown in the IMERG data (Figures 7a–7e), the HREs in the SMALL cases have a precipitation distribution elongated in the east-west or southwest-northeast direction throughout the Korean Peninsula; all five representative cases are accompanied by high-intensity precipitation (>150 mm). The precipitation simulations produced by the KF (Figures 7f–7j) and MSKF (Figures 7k–7o) schemes have similar spatial distributions, which closely resemble the patterns observed in the IMERG data (i.e., long rain band pattern with high intensity). In contrast, the IMERG precipitation distributions in the LARGE cases exhibit localized events with precipitation amounts smaller than those in the SMALL cases (Figures 8a–8e). Both CPSs reveal a tendency to overestimate the simulated rainfall compared with the observed rainfall from IMERG data and simulated false rainfall over regions with no observed precipitation. The difference in the precipitation distributions between the KF and MSKF experiments is more pronounced in the LARGE cases than in the SMALL cases. In addition, predictability tends to be lower in regions with light precipitation than in areas with heavy precipitation.

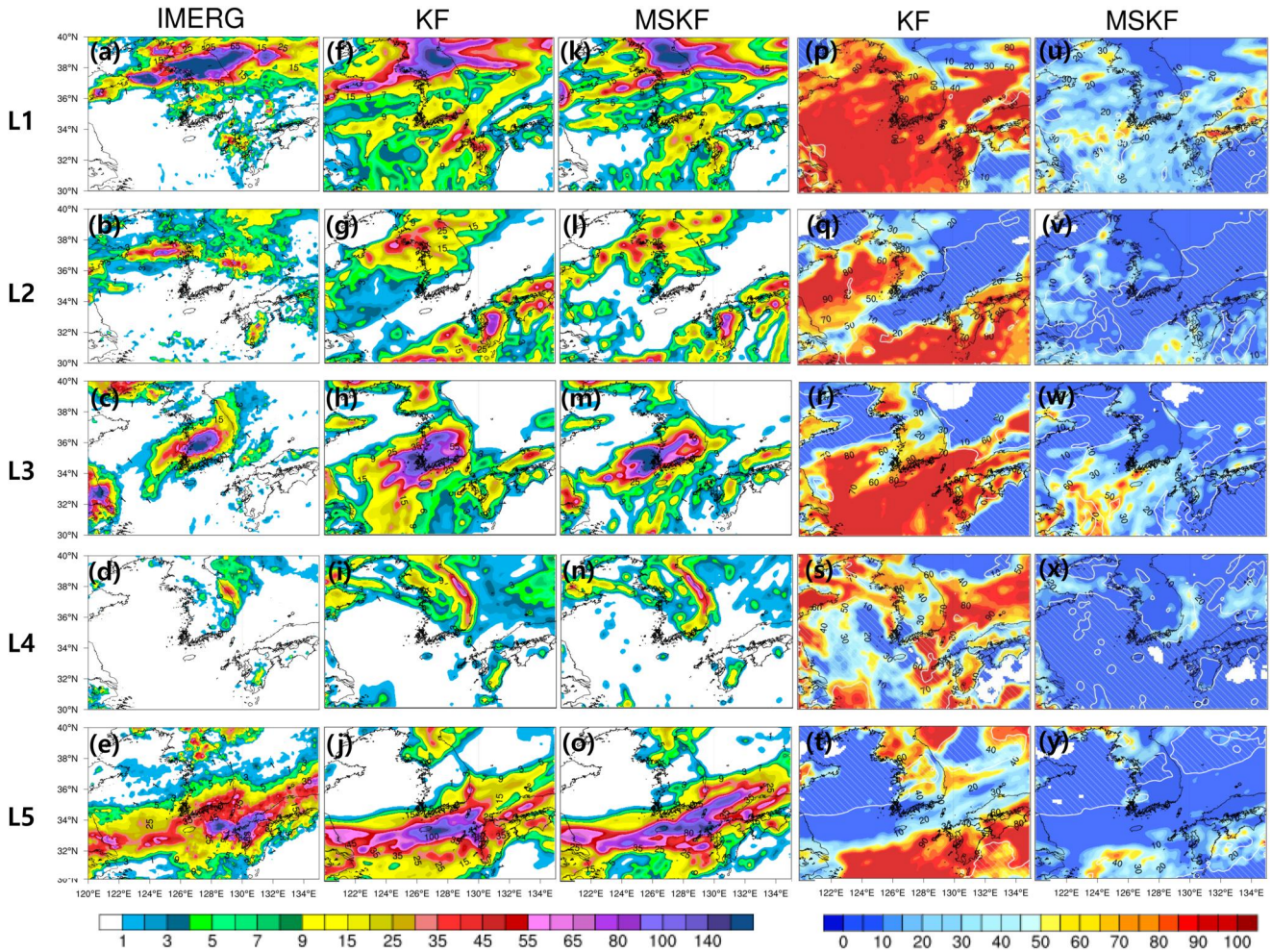

Figure 8. As in Figure 7, but for the HREs in the LARGE cases.

To investigate the cause of the difference in predictability between the SMALL and LARGE cases, we examine the characteristics of simulated precipitation using CRR (p-y in Figures 7 and 8), which is defined as the ratio of subgrid-scale precipitation to total precipitation. As CRR approaches 100%, total precipitation is primarily simulated by CPS rather than MPS. In contrast, as it approaches 0%, simulated precipitation is explicitly resolved by MPS. In the HREs classified as the SMALL cases, the CRR of both experiments is 0%–10% over most areas with total precipitation of more than 30 mm, despite relatively high CRR over the regions with light precipitation (e.g., the southern ocean of the Korean Peninsula). This indicates that both experiments tend to simulate most precipitation as grid-scale precipitation from MPS in the SMALL cases. In the LARGE cases, on the contrary, the two experiments considerably increase CRR. In particular, the KF experiments show a more significant increase in CRR than the MSKF experiments; the KF experiments increase CRR up to 100% over most precipitation areas (Figures 8p–8t), while the CRR in the MSKF experiments is less than 50% (Figures 8u–8y). This means that for the LARGE cases, most precipitation in the KF experiments is simulated as the subgrid-scale precipitation from CPS, but there is a balance between the grid-scale precipitation and subgrid-scale precipitation in the MSKF experiments. It is also noteworthy that the KF experiments tend to overestimate the total precipitation over the regions with high CRR.

Therefore, there is no significant difference between the experimental results of the two schemes for the SMALL cases because large-scale precipitation in the form of intense and long precipitation bands caused by strong synoptic forcings occurred mainly as grid-scale precipitation. However, for the LARGE cases characterized by the local or meso-scale precipitation with weak synoptic forcings, the differences in precipitation characteristics

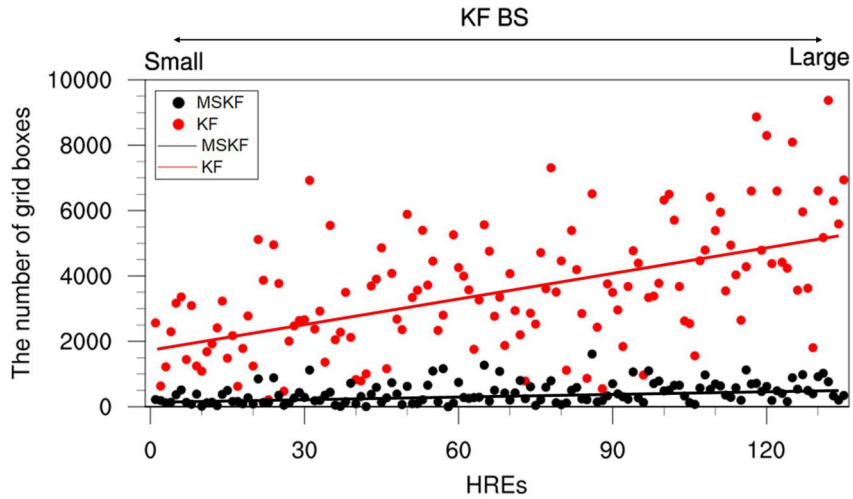

Figure 9. The number of grid boxes is counted when the simulated precipitation in each CPSs (i.e., KF and MSKF schemes) is overestimated than the IMERG data at 5 mm threshold, and the CRR is over 66% (The number of grid boxes are counted for target region between 30 and 45°N and 120–135°E).

(i.e., CRR) between the two experiments are large due to the exaggerated subgrid-scale precipitation by the KF scheme, resulting in a significant difference in total precipitation.

We also count the number of grid boxes where total precipitation for each experiment is overestimated by 5 mm compared to the IMERG data and CRR is greater than 66%, to clarify that the total precipitation bias is related to the characteristics of simulated precipitation (Figure 9). The *x*-axis represents 135 cases sorted in ascending order by the BS of the KF experiments at a 5 mm threshold. The results indicate that both experiments increase the number of counted grid boxes as the BS of the KF experiments increases. However, the KF experiments have a much larger increasing tendency compared to the MSKF experiments. The correlation coefficients of KF and MSKF have values of 0.53 and 0.34, respectively ($p < 0.001$). In addition, the KF experiments have a more pronounced tendency to increase at a lower threshold than a strong threshold (not shown). This suggests that the excessive subgrid-scale precipitation from CPS is responsible for lower predictability in the KF experiments. In contrast, the MSKF scheme reduces the errors in total precipitation by decreasing the subgrid-scale precipitation. This improvement is particularly evident in the light precipitation region (Figure 8). Overall, the results suggest that the MSKF scheme can effectively reduce the excessive subgrid-scale precipitation and improve the performance of simulated precipitation, particularly in light precipitation regions.

4. Summary and Conclusion

This study aims to assess the effect of a scale-aware CPS in improving the forecast accuracy of HREs in the gray-zone. We evaluate the performance of two types of CPSs in the WRF model over the Korean Peninsula. In particular, the KF scheme is used as a non-scale-aware CPS, whereas the MSKF scheme is employed as a scale-aware CPS. This study investigates the impact of CPSs on 135 heavy rainfall events over 10 years from 2011 to 2020 at a grid spacing of 4 km.

The MSKF scheme improves the performance of precipitation simulation compared with the KF scheme. In particular, the KF scheme tends to over-simulate precipitation compared to MSKF scheme at low thresholds (as shown in Figures 2 and 3). Furthermore, our results show that the predictability of the two schemes is affected by lower-level environmental conditions (i.e., wind and water vapor transport) around the Korean Peninsula. It is confirmed that stronger synoptic scale environmental conditions around the Korean Peninsula are generally related to better predictability than weak conditions. In addition, the performance of precipitation simulation between the two schemes is similar as the synoptic forcing conditions around the Korean Peninsula are strong, whereas the performance difference is significant as the synoptic forcings are weak. When the predictability between the two schemes is similar, intense and long rainbands throughout the Korean Peninsula are observed in the IMERG data,

and most of total precipitation is simulated by MPS rather than CPS. However, when the two schemes significantly differ in forecasting, HREs show local or mesoscale precipitation distributions. In addition, the KF scheme tends to overestimate and falsely predict total precipitation because of the excessive simulation of subgrid-scale precipitation from the CPS. However, the MSKF scheme improves the precipitation simulation by increasing grid-scale precipitation and reducing subgrid-scale precipitation overestimated in the KF scheme. Park et al. (2022) suggested that excessive action of the CPS, particularly in what is known as the gray-zone, played a crucial role. This excessive CPS activity led to an exaggeration of convection and the distortion of synoptic fields, notably in high-resolution simulations. Consequently, these distortions result in the overestimation of precipitation, leading to excessive simulated precipitation. Therefore, the different precipitation partitioning simulated between non-scale-aware (KF) and scale-aware (MSKF) schemes during weak-synoptic forcing events can be attributed to the impact of excessive CPS action, as elucidated in the findings by Park et al. (2022).

We find that the precipitation forecast performance of CPS can depend on the type (characteristics) of HREs on the Korean Peninsula. For HREs with strong synoptic conditions over the Korean Peninsula, the forecast performances of the two CPSs (i.e., non-scale-aware and scale-aware) are similar. However, during local heavy rainfall events, we find that the scale-aware parameterization scheme is helpful in improving the prediction of light precipitation in the gray-zone.

Despite numerous studies, the need for CPS near the grid spacing of 5 km remains ambiguous (Deng & Stauffer, 2006; Jee & Kim, 2017; Lee et al., 2011; Liang et al., 2019; McMillen & Steenburgh, 2015; Park et al., 2022). Accordingly, we generalize the predictability of CPS in the gray-zone for 135 HREs over the Korean Peninsula using non-scale-aware and scale-aware CPSs. In addition, we provide insight into the role of scale-aware CPS in the simulation of HREs with weak synoptic forcing. However, our research has a limitation that only KF-based CPSs implemented in the WRF model are tested for HREs occurred in South Korea. Thus, further studies using other scale-aware CPSs (e.g., Scale-aware Grell-Freitas) are required to generalize the necessity of scale-aware CPS in the gray-zone. This study also has the limitation that the sensitivity of the scale-aware CPS to the horizontal resolution could not be analyzed because the two-way nesting method was used and the analysis of results focused on the innermost domain. Therefore, one-way nesting experiments are required to determine the sensitivity of scale-aware CPS to different resolutions. In addition, it is needed to investigate the effect of scale-aware CPS on HREs over other regions. In terms of spatial limitations of the data sets, there is a limitation of relying on only one data set (IMERG) to verify the results obtained by simulating the model. It is also important to note that single initial condition is used. Simulations should be conducted under various initial conditions to reduce the uncertainty caused by initial conditions.

Data Availability Statement

We used the Advanced Research Weather Research and Forecasting (WRF) model Version 4.1 are available at https://github.com/wrf-model/WRF/tree/release-v4.1 (WRF, 2019). Figures have been made with the National Center for Atmospheric Research (NCAR) Command Language (NCL v6.6.1) post-processing tool accessible at https://www.ncl.ucar.edu (http://dx.doi.org/10.5065/D6WD3XH5) (NCAR, 2019). The meteorological input data to create the initial and boundary conditions for the WRF model domains were obtained from the National Centers for Environmental Prediction Global Final Analysis (NCEP-FNL) data are available online at https://rda.ucar.edu/datasets/ds083.2 (FNL, 2000). They were archived at NASA GES DISC (https://disc.gsfc.nasa.gov/datasets/GPM_3IMERGHH_V06/summary) and online https://gpm.nasa.gov/data/directory (IMERG, 2017). Reanalysis file for ERA5 hourly data was downloaded from the National Center for Atmospheric Research's data archive (ERA5, 2018) https://doi.org/10.24381/cds.adbb2d47. The WRF simulation data can be accessed on the Zenodo repository (https://doi.org/10.5281/zenodo.8394470) (Park et al., 2023).

Acknowledgments
This work was supported by the National Research Foundation of Korea Grant funded by the Korean Government (NRF-2022R1F1A1076381), and the Korea Environment Industry & Technology Institute (KEITI) through the "Climate Change R&D Project for New Climate Regime." funded by the Korea Ministry of Environment (MOE) (1485018907). We thank the supercomputing resouces of the UNIST Supercomputing Center.

References

Alapaty, K., Herwehe, J. A., Otte, T. L., Nolte, C. G., Bullock, O. R., Mallard, M. S., et al. (2012). Introducing subgrid-scale cloud feedbacks to radiation for regional meteorological and climate modeling. *Geophysical Research Letters*, *39*(24), 2012GL054031. https://doi.org/10.1029/2012GL054031

Arakawa, A., Jung, J. H., & Wu, C. M. (2011). Toward unification of the multiscale modeling of the atmosphere. *Atmospheric Chemistry and Physics*, *11*(8), 3731–3742. https://doi.org/10.5194/acp-11-3731-2011

Bengtsson, L., & Körnich, H. (2016). Impact of a stochastic parametrization of cumulus convection, using cellular automata, in a mesoscale ensemble prediction system. *Quarterly Journal of the Royal Meteorological Society*, *142*(695), 1150–1159. https://doi.org/10.1002/qj.2720

Charles, M. E., & Colle, B. A. (2009). Verification of extratropical cyclones within the NCEP operational models. Part I: Analysis errors and short-term NAM and GFS forecasts. *Weather and Forecasting*, *24*(5), 1173–1190. https://doi.org/10.1175/2009waf2222169.1

Chen, F., & Dudhia, J. (2001). Coupling an advanced land surface–hydrology model with the Penn State–NCAR MM5 modeling system. Part I: Model implementation and sensitivity. *Monthly Weather Review*, *129*(4), 569–585. https://doi.org/10.1175/1520-0493(2001)129<0569:caalsh>2.0.co;2

Chen, G. T. J., & Yu, C. C. (1988). Study of low-level jet and extremely heavy rainfall over northern Taiwan in the mei-yu season. *Monthly Weather Review*, *116*(4), 884–891. https://doi.org/10.1175/1520-0493(1988)116<0884:sollja>2.0.co;2

Cho, N. S., & Lee, T. Y. (2006). A numerical study of multiple convection bands over the Korean peninsula. *Asia-Pacific Journal of Atmospheric Sciences*, *42*(2), 87–105.

Davies, T., Cullen, M. J., Malcolm, A. J., Mawson, M. H., Staniforth, A., White, A. A., & Wood, N. (2005). A new dynamical core for the Met Office's global and regional modelling of the atmosphere. *Quarterly Journal of the Royal Meteorological Society: A Journal of the Atmospheric Sciences, Applied Meteorology and Physical Oceanography*, *131*(608), 1759–1782. https://doi.org/10.1256/qj.04.101

Deng, A., & Stauffer, D. R. (2006). On improving 4-km mesoscale model simulations. *Journal of Applied Meteorology and Climatology*, *45*(3), 361–381. https://doi.org/10.1175/jam2341.1

Deuk-Kyun, R., Myoung-Seok, S., & Yoon, H. (2005). Analysis of the characteristics of precipitation over South Korea in terms of the associated synoptic patterns: A 30 years climatology (1973~ 2002). *Journal of the Korean Earth Science Society*, *26*(7), 732–743.

Dudhia, J. (1989). Numerical study of convection observed during the winter monsoon experiment using a mesoscale two-dimensional model. *Journal of the Atmospheric Sciences*, *46*(20), 3077–3107. https://doi.org/10.1175/1520-0469(1989)046<3077:nsocod>2.0.co;2

Ek, M. B., Mitchell, K. E., Lin, Y., Rogers, E., Grunmann, P., Koren, V., et al. (2003). Implementation of Noah land surface model advances in the National Centers for Environmental Prediction operational mesoscale Eta model. *Journal of Geophysical Research*, *108*(D22), 8851. https://doi.org/10.1029/2002jd003296

ERA5. (2018). ERA5 hourly data on pressure levels from 1959 to present [Dataset]. *Copernicus/ECMWF. Re*. Retrieved from https://cds.climate.copernicus.eu/cdsapp#!/dataset/

FNL (2000), National Centers for Environmental Prediction/National Weather Service/NOAA/U.S. Department of Commerce. (2000). NCEP FNL operational model global tropospheric analyses, continuing from July 1999 (updated daily) [Dataset]. *Research Data Archive at the National Center for Atmospheric Research, Computational and Information Systems Laboratory*. https://doi.org/10.5065/D6M043C6

Gerard, L., Piriou, J. M., Brožková, R., Geleyn, J. F., & Banciu, D. (2009). Cloud and precipitation parameterization in a meso-gamma-scale operational weather prediction model. *Monthly Weather Review*, *137*(11), 3960–3977. https://doi.org/10.1175/2009mwr2750.1

Grell, G. A., & Freitas, S. R. (2014). A scale and aerosol aware stochastic convective parameterization for weather and air quality modeling. *Atmospheric Chemistry and Physics*, *14*(10), 5233–5250. https://doi.org/10.5194/acp-14-5233-2014

Han, J., Wang, W., Kwon, Y. C., Hong, S. Y., Tallapragada, V., & Yang, F. (2017). Updates in the NCEP GFS cumulus convection schemes with scale and aerosol awareness. *Weather and Forecasting*, *32*(5), 2005–2017. https://doi.org/10.1175/waf-d-17-0046.1

Han, J. Y., & Hong, S. Y. (2018). Precipitation forecast experiments using the Weather Research and Forecasting (WRF) Model at gray-zone resolutions. *Weather and Forecasting*, *33*(6), 1605–1616. https://doi.org/10.1175/waf-d-18-0026.1

Hersbach, H., Bell, B., Berrisford, P., Hirahara, S., Horányi, A., Muñoz-Sabater, J., et al. (2020). The ERA5 global reanalysis. *Quarterly Journal of the Royal Meteorological Society*, *146*(730), 1999–2049. https://doi.org/10.1002/qj.3803

Hong, S. Y. (2004). Comparison of heavy rainfall mechanisms in Korea and the central US. *Journal of the Meteorological Society of Japan. Ser. II*, *82*(5), 1469–1479. https://doi.org/10.2151/jmsj.2004.1469

Hong, S. Y., & Dudhia, J. (2012). Next-generation numerical weather prediction: Bridging parameterization, explicit clouds, and large eddies. *Bulletin of the American Meteorological Society*, *93*(1), ES6–ES9. https://doi.org/10.1175/2011bams3224.1

Hong, S. Y., & Lim, J. O. J. (2006). The WRF single-moment 6-class microphysics scheme (WSM6). *Asia-Pacific Journal of Atmospheric Sciences*, *42*(2), 129–151.

Hong, S. Y., Noh, Y., & Dudhia, J. (2006). A new vertical diffusion package with an explicit treatment of entrainment processes. *Monthly Weather Review*, *134*(9), 2318–2341. https://doi.org/10.1175/mwr3199.1

Huffman, G. J., Bolvin, D. T., Braithwaite, D., Hsu, K., Joyce, R., Xie, P., & Yoo, S.-H. (2015). NASA global precipitation measurement (GPM) integrated multi-satellite retrievals for GPM (IMERG) (Vol. *4*, p. 26).

Huffman, G. J., Bolvin, D. T., Nelkin, E. J., & Tan, J. J. (2015). Integrated Multi-satellitE Retrievals for GPM (IMERG) technical documentation (Vol. *612*(47)), 2019.

Hwang, L. (1993). A study on the relationship between heavy rainfalls and associated low-level jets in the Korean Peninsula. *Asia-Pacific Journal of Atmospheric Sciences*, *29*(2), 133–146.

IMERG. (2017). GPM IMERG final precipitation L3 half hourly 0.1 degree× 0.1 degree V05. *Goddard Earth Sciences Data and Information Services Center (GES DISC)*. https://doi.org/10.5067/GPM/IMERG/3B-HH/06

Jee, J. B., & Kim, S. (2017). Sensitivity study on high-resolution WRF precipitation forecast for a heavy rainfall event. *Atmosphere*, *8*(6), 96. https://doi.org/10.3390/atmos8060096

Jeong, G. Y., & Ryu, C. S. (2008). The synoptic characteristics of heavy rain in South Korea. *Journal of the Chosun Natural Science*, *1*(2), 89–114.

Kain, J. S. (2004). The Kain–Fritsch convective parameterization: An update. *Journal of Applied Meteorology*, *43*(1), 170–181. https://doi.org/10.1175/1520-0450(2004)043<0170:tkcpau>2.0.co;2

Kim, Y.-T., Park, M., & Kwon, H.-H. (2020). Spatio-Temporal summer rainfall pattern in 2020 from a rainfall frequency perspective. *Journal of Korean Society of Disaster and Security*, *13*(4), 93–104. https://doi.org/10.21729/ksds.2020.13.4.93

Kwon, Y. C., & Hong, S. Y. (2017). A mass-flux cumulus parameterization scheme across gray-zone resolutions. *Monthly Weather Review*, *145*(2), 583–598. https://doi.org/10.1175/mwr-d-16-0034.1

Lee, S. W., Lee, D. K., & Chang, D. E. (2011). Impact of horizontal resolution and cumulus parameterization scheme on the simulation of heavy rainfall events over the Korean Peninsula. *Advances in Atmospheric Sciences*, *28*, 1–15. https://doi.org/10.1007/s00376-010-9217-x

Lee, T. Y., & Kim, Y. H. (2007). Heavy precipitation systems over the Korean peninsula and their classification. *Asia-Pacific Journal of Atmospheric Sciences*, *43*(4), 367–396.

Liang, X. Z., Li, Q., Mei, H., & Zeng, M. (2019). Multi-grid nesting ability to represent convections across the gray zone. *Journal of Advances in Modeling Earth Systems*, *11*(12), 4352–4376. https://doi.org/10.1029/2019ms001741

Matsumoto, S. (1973). Lower tropospheric wind speed and precipitation activity. *Journal of the Meteorological Society of Japan. Ser. II*, *51*(2), 101–107. https://doi.org/10.2151/jmsj1965.51.2_101

McMillen, J. D., & Steenburgh, W. J. (2015). Impact of microphysics parameterizations on simulations of the 27 October 2010 Great Salt Lake–effect snowstorm. *Weather and Forecasting*, *30*(1), 136–152. https://doi.org/10.1175/waf-d-14-00060.1

Mlawer, E. J., Taubman, S. J., Brown, P. D., Iacono, M. J., & Clough, S. A. (1997). Radiative transfer for inhomogeneous atmospheres: RRTM, a validated correlated-k model for the longwave. *Journal of Geophysical Research*, *102*(D14), 16663–16682. https://doi.org/10.1029/97jd00237

NCAR. (2019). *The NCAR command language*. UCAR/NCAR/CISL/TDD. https://doi.org/10.5065/D6WD3XH5

Noh, Y., Cheon, W. G., Hong, S. Y., & Raasch, S. (2003). Improvement of the K-profile model for the planetary boundary layer based on large eddy simulation data. *Boundary-Layer Meteorology*, *107*(2), 401–427. https://doi.org/10.1023/a:1022146015946

Park, H., Hwang, J., Cha, D. H., Lee, M. I., Song, C. K., Kim, J., et al. (2023). WRF simulation data. *Zenodo repository*, *14*(6). https://doi.org/10.5281/zenodo.8394470

Park, H., Kim, G., Cha, D. H., Chang, E. C., Kim, J., Park, S. H., & Lee, D. K. (2022). Effect of a scale-aware convective parameterization scheme on the simulation of convective cells-related heavy rainfall in South Korea. *Journal of Advances in Modeling Earth Systems*, *14*(6), e2021MS002696. https://doi.org/10.1029/2021ms002696

Park, S. (2014). A unified convection scheme (UNICON). Part I: Formulation. *Journal of the Atmospheric Sciences*, *71*(11), 3902–3930. https://doi.org/10.1175/jas-d-13-0233.1

Prein, A. F., Langhans, W., Fosser, G., Ferrone, A., Ban, N., Goergen, K., et al. (2015). A review on regional convection-permitting climate modeling: Demonstrations, prospects, and challenges. *Reviews of Geophysics*, *53*(2), 323–361. https://doi.org/10.1002/2014rg000475

Ren, X., Yang, D., & Yang, X. Q. (2015). Characteristics and mechanisms of the subseasonal eastward extension of the South Asian high. *Journal of Climate*, *28*(17), 6799–6822. https://doi.org/10.1175/jcli-d-14-00682.1

Saito, K., Fujita, T., Yamada, Y., Ishida, J. I., Kumagai, Y., Aranami, K., et al. (2006). The operational JMA nonhydrostatic mesoscale model. *Monthly Weather Review*, *134*(4), 1266–1298. https://doi.org/10.1175/mwr3120.1

Seo, K. H., Son, J. H., & Lee, J. Y. (2011). A new look at Changma. *Atmosphere*, *21*, 109–121. In Korean with English abstract.

Shin, C. S., & Lee, T. Y. (2005). Development mechanisms for the heavy rainfalls of 6-7 August 2002 over the middle of the Korean Peninsula. *Journal of the Meteorological Society of Japan. Ser. II*, *83*(5), 683–709. https://doi.org/10.2151/jmsj.83.683

Skamarock, W. C., Klemp, J. B., Dudhia, J., Gill, D. O., Liu, Z., Berner, J., et al. (2019). *A description of the advanced research WRF model version 4* (Vol. 145). National Center for Atmospheric Research.

Sun, J., & Lee, T. Y. (2002). A numerical study of an intense quasi-stationary convection band over the Korean Peninsula. *Journal of the Meteorological Society of Japan. Ser. II*, *80*(5), 1221–1245. https://doi.org/10.2151/jmsj.80.1221

Wilks, D. S. (2011). *Statistical methods in the atmospheric sciences* (Vol. 100). Academic press.

WRF. (2019). A description of the advanced research WRF model version 4 [Software]. WRF. Retrieved from https://www2.mmm.ucar.edu/wrf/users/download/get_source.html

Yun, Y., Fan, J., Xiao, H., Zhang, G. J., Ghan, S. J., Xu, K. M., et al. (2017). Assessing the resolution adaptability of the Zhang-McFarlane cumulus parameterization with spatial and temporal averaging. *Journal of Advances in Modeling Earth Systems*, *9*(7), 2753–2770. https://doi.org/10.1002/2017ms001035

Zheng, Y., Alapaty, K., Herwehe, J. A., Del Genio, A. D., & Niyogi, D. (2016). Improving high-resolution weather forecasts using the weather research and forecasting (WRF) model with an updated Kain–Fritsch scheme. *Monthly Weather Review*, *144*(3), 833–860. https://doi.org/10.1175/mwr-d-15-0005.1